

Mechanical Basis and Topological Routes to Cell Elimination

Siavash Monfared,¹ Guruswami Ravichandran,² José E. Andrade,² and Amin Doostmohammadi²

¹*Division of Engineering and Applied Science, California Institute of Technology, Pasadena, CA 91125, USA.*

²*Niels Bohr Institute, University of Copenhagen, Denmark.*

Cell layers eliminate unwanted cells through the extrusion process, which underlines healthy versus flawed tissue behaviors. Although several biochemical pathways have been identified, the underlying mechanical basis including the forces involved in cellular extrusion remain largely unexplored. Utilizing a phase-field model of a three-dimensional cell layer, we study the interplay of cell extrusion with cell-cell and cell-substrate interactions, in a flat monolayer. Independent tuning of cell-cell versus cell-substrate adhesion forces reveals that extrusion events can be distinctly linked to defects in nematic and hexatic orders associated with cellular arrangements. Specifically, we show that by increasing relative cell-cell adhesion forces the cell monolayer can switch between the collective tendency towards five-fold, hexatic, disclinations relative to half-integer, nematic, defects for extruding a cell. We unify our findings by accessing three-dimensional mechanical stress fields to show that an extrusion event acts as a mechanism to relieve localized stress concentration.

INTRODUCTION

The ability of cells to self-organize and to collectively migrate drives numerous physiological processes including morphogenesis [1, 2], epithelial-mesenchymal transition [3], wound healing [4], and tumor progression [5]. Advanced experimental techniques have linked this ability to mechanical interactions between cells [6–8]. Specifically, cells actively coordinate their movements through mechanosensitive adhesion complexes at the cell-substrate interface and cell-cell junctions. Moreover, cell-cell and cell-substrate adhesions seem to be coupled [9], further complicating the interplay of mechanics with biochemistry.

While advances in experimental techniques are followed by more nuanced theoretical and computational developments, a majority of current approaches to simulate multicellular layers are limited to two-dimensional systems, hindering in-depth exploration of intrinsically three-dimensional nature of the distinct forces that govern cell-cell and cell-substrate interactions. Furthermore, some of the most fundamental processes in cell biology such as cell extrusion - responsible for tissue integrity - are inherently three-dimensional. Thus, studying the underlying mechanisms necessitates access to both in-plane and out-of-plane forces in the cell layers.

Cell extrusion refers to the process of removal of excess cells to prevent accumulation of unnecessary or pathological cells [10]. This process can get initiated through apoptotic signaling [10], oncogenic transformation [11], and overcrowding of cells [12–14] or induced by replication stress [15]. Most importantly, cell extrusion plays an important role in developmental [16], homeostatic [13, 17] and pathological processes [18], including cancer metastasis. However, the underlying mechanisms that facilitate cell extrusion are still unclear.

The similarities between cellular systems and liquid crystals, studied both theoretically and experimentally, featuring both nematic order [19–24] and hexatic order

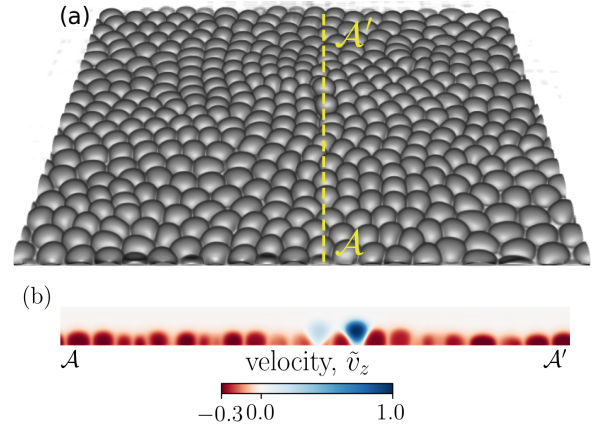


Figure 1. **Cell extrusion in a 3D representation of a confluent cell layer.** (a): A representative simulation snapshot (cell-substrate adhesion $\omega_{cw} = 0.0025$ and relative cell-cell adhesion $\Omega = \omega_{cc}/\omega_{cw} = 0.4$) of a three-dimensional cell monolayer. Two cells are visibly extruding. (b): A cross-section (dotted yellow line $\mathcal{A} - \mathcal{A}'$) of the cell monolayer highlighting the two extruding cells via the normalized out-of-plane velocity ($\tilde{v}_z = (\vec{v} \cdot \vec{e}_z)/v_z^{\max}$), where v_z^{\max} is the maximum value of the v_z component of the velocity field \vec{v} in the shown cross-section.

[25–29] with the two phases potentially coexisting [30] and interacting provide a fresh perspective for understanding cellular processes. The five-fold disclinations in hexatic arrangement of cells are numerically shown to favor overlaps between the cells in two-dimensions [31], potentially contributing to the cell extrusion in three-dimensions. In this vein, it is shown that a net positive charge associated with hexatic disclinations can be associated with the maximum curvature of dome-like structures in model organoids and in epithelial cell layers [29, 32, 33]. Moreover, in cellular monolayers, comet- and trefoil-shaped half-integer topological defects, cor-

responding to $+1/2$ and $-1/2$ charges, respectively, are prevalent [34, 35]. These are singular points in cellular alignment that mark the breakdown of orientational order [36]. Recent experiments on epithelial monolayers found a strong correlation between extrusion events and the position of a subset of $+1/2$ defects in addition to a relatively weaker correlation with $-1/2$ defects [19]. These recently introduced purely mechanical routes to cell extrusion have opened the door to new questions on the nature of forces that are involved in eliminating cells from the monolayer and challenge the purely biological consensus that an extruding cell sends a signal to its neighbor that activates its elimination process [10]. Nevertheless, it is not clear if these different mechanisms are related, and whether, depending on the mechanical features of the cells, the cell layers actively switch between different routes to eliminate the unwanted cells. Since all the existing studies so far have only focused on effective two-dimensional models of the cell layers, fundamental questions about the three-dimensional phenomenon of cell extrusion and its connection to the interplay between cell-generated forces at the interface between cells and the substrate, with multicellular force transmission across the cell layer, remain unanswered.

In this article, we explore three-dimensional collective cell migration in cellular monolayers. Based on large scale simulations, we examine (i) the underlying mechanisms responsible for cell extrusion, including any correlations with $\pm 1/2$ topological defects and five-fold disclinations, and (ii) the interplay of cell-cell and cell-substrate adhesion with extrusion events in cellular systems. Moreover, by mapping the full three-dimensional mechanical stress field across the entire monolayer, we identify localized stress concentration as the unifying factor that governs distinct topological routes to cell extrusion.

RESULTS AND DISCUSSIONS

Topological routes to cell extrusion: nematic and hexatic disclinations

In the absence of self-propulsion forces, the initial configuration tends to equilibrate into a hexagonal lattice (see Fig. 16 in SI for an example). As we introduce self-propulsion forces associated with front-rear cell polarity (see Methods for polarisation dynamics), the system is pushed away from its equilibrium hexagonal configuration, resulting in defects manifested as five-fold and seven-fold disclinations, as shown in Fig. 2(b). Fig. 1(a) shows a simulation snapshot with two extrusion events taking place. An extrusion event is detected if the vertical displacement of a cell, relative to other cells in the monolayer, exceeds $R_0/2$, where R_0 is the initial cell radius. Fig. 1(b) displays the out-of-plane normalized

velocity profile, $\vec{v}_z = (\vec{v}(\vec{x}) \cdot \vec{e}_z) / v_z^{\max}$ where v_z^{\max} is the maximum value of the velocity component in \vec{e}_z direction in the displayed cross-section of the monolayer, clearly marking the extruding cells as they get expelled from the monolayer and lose contact with the substrate.

In order to probe the possible mechanical routes to cell extrusion, we begin with characterizing topological defects in cell orientation field and disclinations in cellular arrangements. To this end, we first map the orientation field of the cells from the 2D projected cell shape profile on xy -plane ($z = 0$, i.e. the basal side) and identify topological defects as the singularities in the orientation field. The results (example snapshot in Fig. 2a) show the continuous emergence of half-integer ($\pm 1/2$), nematic, topological defects that spontaneously nucleate in pairs and follow chaotic trajectories before annihilation (see Fig. 14 in SI for energy spectra characterization). It is noteworthy that unlike previous studies of active nematic behavior in 2D cell layers [37, 38], the nematic defects here emerge in the absence of any active dipolar stress or subcellular fields, as the only active driving in these simulations is the polar force that the cells generate. Therefore, although the cells are endowed with polarity in terms of their self-propulsion, the emergent symmetry in terms of their orientational alignment is nematic, which is inline with experimental observations in cell monolayers [19, 22], discrete models of self-propelled rods [39, 40], and recently proposed continuum model of polar active matter [41].

Remarkably, in accordance with experimental observations [19], we find that the extrusion events can be correlated with the position of both $+1/2$ comet-shaped and $-1/2$ trefoil-shaped topological defects. To quantify this, Figs. 2(c)-(d) display the probability density of the normalized minimum distance $\tilde{d}_{\min}^{\pm 1/2} = d_{\min}^{\pm 1/2} / R_0$ between an extruding cell and $\pm 1/2$ topological defects in the interval $\tilde{t} \in [\tilde{t}_e - 5.625, \tilde{t}_e + 0.625]$, where $\tilde{t} = t / \tau_0$ is the normalized time, $\tau_0 = \xi R_0 / \alpha$, ξ corresponds to cell-substrate friction, α denotes the strength of polarity force and \tilde{t}_e is the (normalized) extrusion time. This temporal window is chosen based on the first moment of a defect's lifetime distribution (see Fig. 10 in SI). The data in Figs. 2(c)-(d) is based on four distinct realizations and for varying cell-substrate to cell-cell adhesion ratios, $\Omega = \omega_{cc} / \omega_{cw}$. For both defect types, the probability density peaks in the vicinity of the eliminated cell ($\approx 1.5R_0$), at a much smaller distance relative to a typical distance between two defects (see Fig. 12 in SI), and falls off to nearly zero for $\tilde{d}_{\min}^{\pm 1/2} \gtrsim 5R_0 (= 40)$. Furthermore, laser ablation experiments have established that an induced extrusion event does not favor the nucleation of a pair of nematic defects [19].

In a hypothesis-testing approach, we check whether these peaks in the minimum distance represent a correlation between extrusion events and nematic defects.

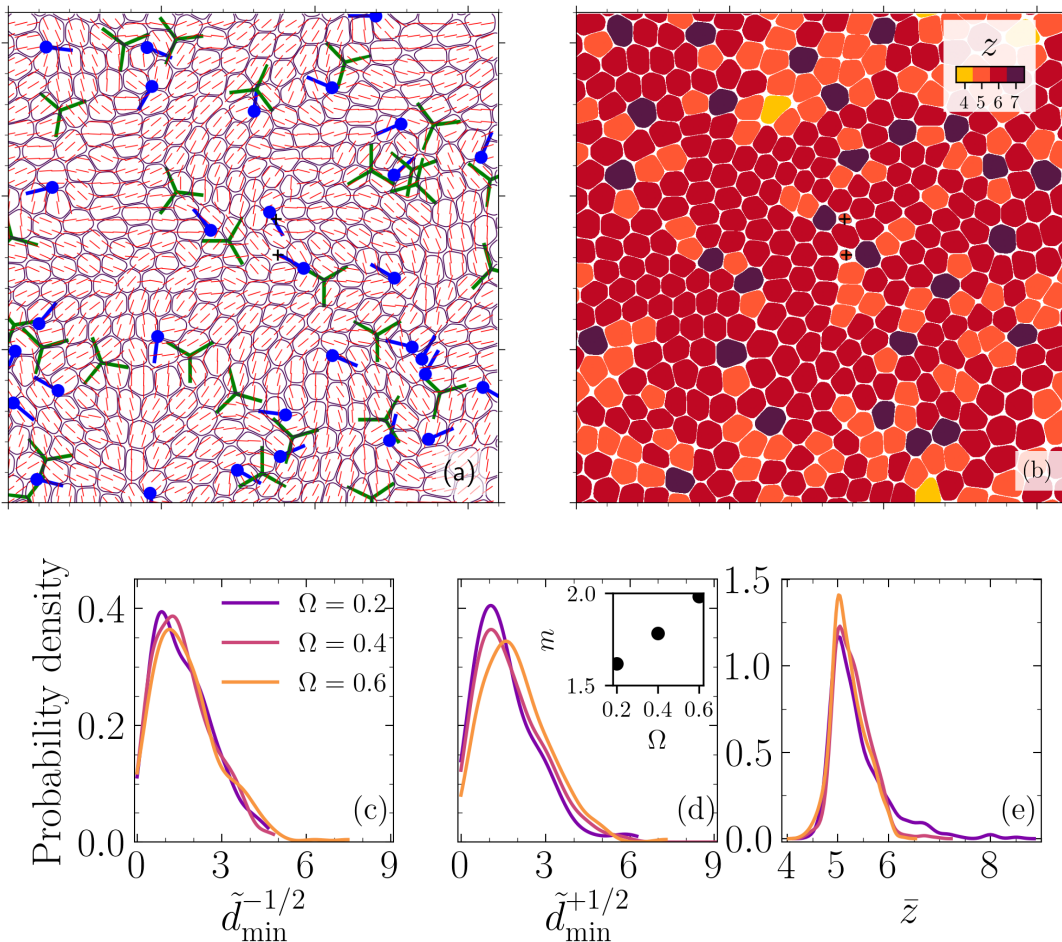


Figure 2. Nematic and hexatic disclinations govern cell extrusion. A representative analysis corresponding to the configuration shown in Fig. 1(a) and projected into xy - plane ($z = 0$, i.e. the basal side). (a): a coarse-grained director field with coarse-graining length of one cell size $\ell_{\text{dir.}} = R_0$ and $+1/2$ (filled circles with the line indicating orientation) and $-1/2$ (three connected lines with 3-fold symmetry) nematic defects. (b): Number of neighbors z for each cell, including five-fold and seven-fold disclinations mapped into the monolayer. The symbol $+$ denotes the center of mass for two extruding cells. (c,d): Probability densities of the normalized minimum distance between extruding cells and the nearest $\pm 1/2$ defect, $\tilde{d}_{\min} = d_{\min}/R_0$, for varying cell-cell to cell-substrate adhesion ratios Ω for (c) $-1/2$ and (d) $+1/2$ topological defects (inset: distribution mean $m = \langle \tilde{d}_{\min}^{+1/2} \rangle$ vs. Ω). (e): The probability density of average coordination number \bar{z} for an extruding cell during $\hat{t} = (t/\tau_0) \in [\hat{t}_e - 2.5, \hat{t}_e + 0.3125]$, where \hat{t}_e denotes extrusion time, $\tau_0 = \xi R_0/\alpha$ and for varying cell-substrate to cell-cell adhesion ratios Ω . The data in (c)-(e) corresponds to four different realizations.

To this end, we set out to falsify the hypothesis that the extrusion events are uncorrelated with the nematic defects. We utilize a poisson point process to randomly generate positions for extrusion events and quantify the minimum distance between each event and the nearest half-integer nematic defect. For each simulation, we generate five different realizations for the extrusion events using a poisson point process with the intensity set equal to the number of extrusions in that particular simulation. The extrusion time is also a random variable described by a uniform distribution, $t_e \sim U(1, n_{\text{sim}})$, where $n_{\text{sim}} = 29,000$ is total number of time steps. As an example, Fig. 3(a) shows probability density function for

$\tilde{d}_{\min}^{+1/2}$ for $\Omega = 0.4$, using simulation data as well as data randomly generated with poisson point process. Finally, a Kolmogorov-Smirnov (KS) test is used to measure if the two samples, one based on our simulations and one based on randomly generated extrusion events, belong to the same distribution. The results of the KS test rejects this (see Tab. I and Fig. 6 in SI) and thus falsifies the hypothesis that simulation based extrusion events are uncorrelated with the half-integer nematic defects.

Next, we explore the other possible mechanical route to cell extrusion based on the disclinations in cellular arrangement. To this end, we compute the coordination number of each cell based on their phase-field interactions

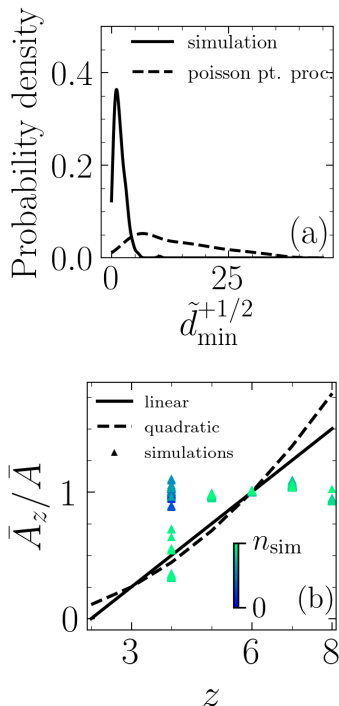


Figure 3. **Topological, rather than geometrical, route to cell extrusion.** (a): Probability density functions for normalized minimum distance between an extrusion event and a $+1/2$ defect, $\tilde{d}_{\min}^{+1/2}$, based on simulation results and randomly generated through a Poisson point process and for $\Omega = 0.4$. (b): comparison of Lewis's linear and quadratic relations with our simulations. \bar{A}_z is the average area for cells with z neighbors and \bar{A} is the average area of all cells. The colorbar indicates simulation time step and the data correspond to the case $\omega_{\text{cw}} = 0.0025$ and $\Omega = 0.4$.

and identify the five-fold and seven-fold disclinations (see Fig. 2(b)). To quantify the relation between extrusion events and the disclinations, the probability density of the coordination number of an extruding cell ($\tilde{d}_{\min} = 0$) averaged over the time interval, $\tilde{t} \in [\tilde{t}_e - 5.625, \tilde{t}_e + 0.625]$, \bar{z} , for all the realizations is shown in Fig. 2(e), clearly exhibiting a sharp peak near $\bar{z} = 5$. The coordination number is determined based on the interactions of cells (see SI) and this property is independent of apical or basal considerations [42], unlike geometrical structures called scutoids that have been identified in curved epithelial tubes [43]. In our setup, the asymmetric interactions of cells with apical and basal sides are captured by varying the strength of cell-substrate adhesion. In our simulations, increasing cell-substrate adhesion leads to lower extrusion events (see Fig. 13 in SI).

Thus far, our results suggest topological rather than geometrical routes to cell extrusion. To probe the role of geometrical constraints further, we investigate the existence of any correlation between cell area and its number of neighbors. The best known such a correlation - for cellular matter with no gaps between them, i.e. con-

fluent state - is a linear one and it is due to F. Lewis [44] with other types of relations, e.g. quadratic, proposed since his work [45]. We compare our simulation results against both the linear ($\bar{A}_z/\bar{A} = (z-2)/4$ where \bar{A}_z is the average area of cell with z neighbors and \bar{A} is the average area of all cells) and quadratic relations ($\bar{A}_z/\bar{A} = (z/6)^2$) and find the agreement poor, as shown for the case of $\omega_{\text{cw}} = 0.0025$ and $\Omega = 0.4$ in Fig. 3(b) (see also Figs. 7 and 8 in SI). While in our simulations the cell monolayers are not always confluent due to the extrusion events, other studies with confluent cellular layers have also found the such relations to not be valid [46, 47]. In our simulations, the projected area of an extruding cell decreases prior to extrusion, but the number of interacting neighbors generally does not change in that time frame (see Fig. 8 in SI). Together, these results suggest mechanical rather than geometrical routes to cell extrusion. Specifically, in our approach cell extrusion emerges as a consequence of cells pushing and pulling on their neighbors due to their intrinsic activity. This contrasts with inherently threshold-based vertex models (see e.g. [48]), for both cellular rearrangements (T1 transitions) and extrusions (T2 transitions).

Mechanical stress localization unifies distinct topological routes to cell extrusion

The correlation between disclinations and extrusion events is also related to the mechanical stress localization at the five-fold disclinations: The occurrence of disclinations in a flat surface produces local stress concentration [49]. Generally, it is energetically favorable to bend a flat surface, rather than to compress or to stretch it [50]. Thus, the local stress concentration can lead to a five-fold (positive Gaussian curvature) or a seven-fold (negative Gaussian curvature) disclination [51, 52]. In our set-up and given that we consider a rigid substrate, five-fold disclinations are much more likely to provide relief for the high local stress concentration. This can change if the rigidity of substrate is relaxed or extrusion in three-dimensional spheroids are considered. Since we conjecture that both topological defect- and disclination-mediated extrusion mechanisms are closely linked with stress localization, we characterize the in-plane and out-of-plane stresses associated with the simulated monolayer. We compute a coarse-grained stress field [53, 54], $\sigma_{ij} = (1/(2V_{\text{cg}})) \sum_{m \in V_{\text{cg}}} (\bar{T}_i(\vec{x}_m) \otimes \vec{e}_j^n + \bar{T}_j(\vec{x}_m) \otimes \vec{e}_i^n)$ where \vec{x}_0 represents the center of the coarse-grained volume, $V_{\text{cg}} = \ell_{\text{stress}}^3$, corresponding to coarse-grained length ℓ_{stress} and unit vector $\vec{e}_i^n = (\vec{x}_0 - \vec{x}_m)/|\vec{x}_0 - \vec{x}_m|$. Herein, the stress fields are computed using $\ell_{\text{stress}} = R_0/4$.

For the example simulation snapshot displayed in Fig. 1(a), at the onset of two extrusion events, we visualize

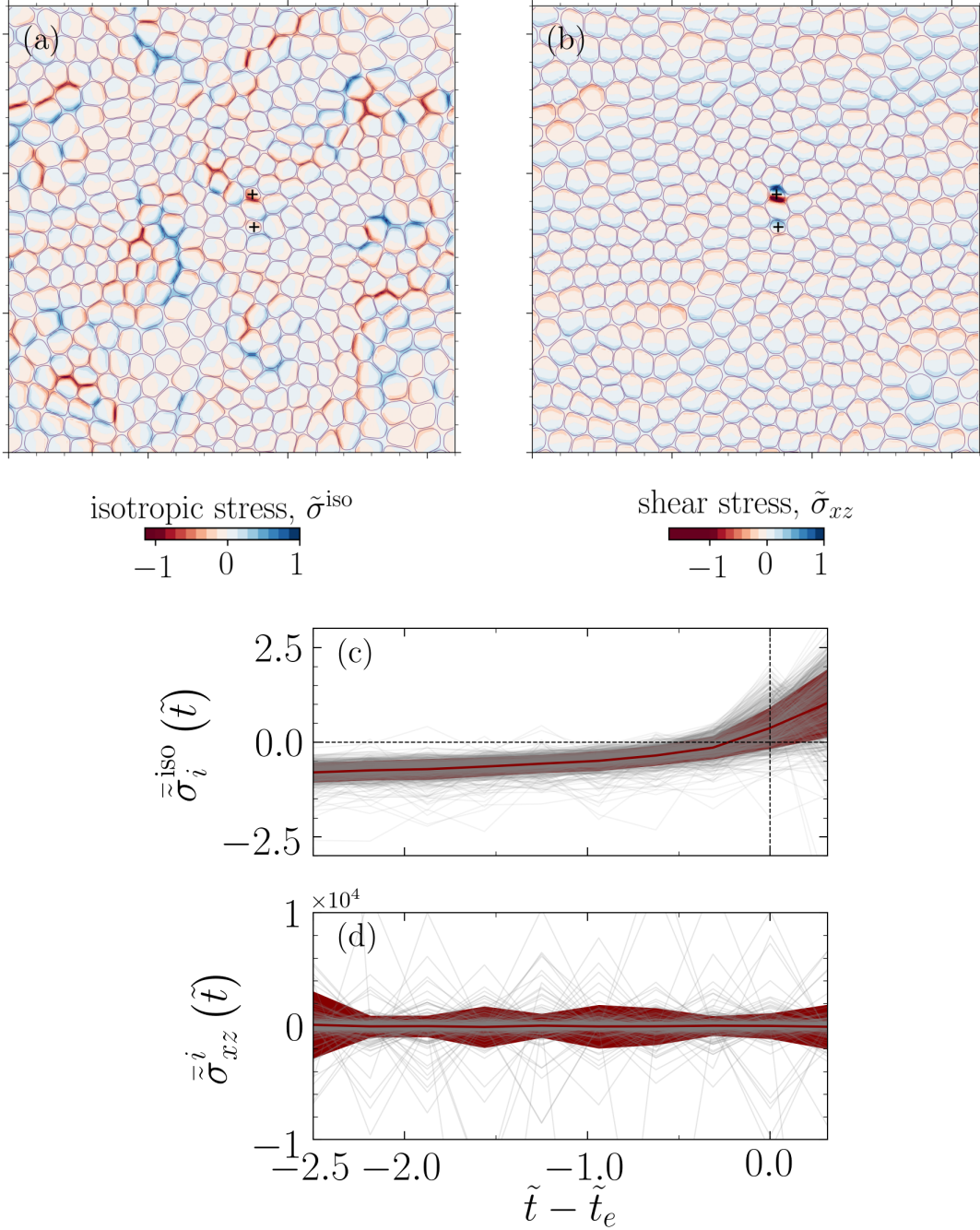


Figure 4. **Temporal build-up of mechanical stress before extrusion events.** A representative analysis corresponding to the configuration shown in Fig. 1(a) and projected into xy -plane ($z = 0$, i.e. the basal side). (a): Normalized isotropic stress field $\tilde{\sigma}^{\text{iso}}(\vec{x}) = \sigma^{\text{iso}}(\vec{x})/\sigma_{\text{max}}^{\text{iso}}$ where $\sigma_{\text{max}}^{\text{iso}}$ is the maximum value of the isotropic stress field and (b) normalized shear stress field, $\tilde{\sigma}_{xz}(\vec{x}) = \sigma_{xz}(\vec{x})/\sigma_{xz}^{\text{max}}$, where σ_{xz}^{max} is the maximum value of $\sigma_{xz}(\vec{x})$ field. The symbol + denotes the center of mass for two extruding cells. (c): cell (spatially) averaged normalized isotropic stress $\bar{\sigma}_i^{\text{iso}}(\tilde{t}) = \langle \sigma^{\text{iso}}(\vec{x}, \tilde{t}) \rangle_{\vec{x} \in \mathcal{R}_i} / \langle \sigma^{\text{iso}}(\vec{x}, \tilde{t}) \rangle_{\vec{x} \in \mathcal{R}}$ and (d) shear stress $\bar{\sigma}_{xz}^i(\tilde{t}) = \langle \sigma_{xz}(\vec{x}, \tilde{t}) \rangle_{\vec{x} \in \mathcal{R}_i} / \langle \sigma_{xz}(\vec{x}, \tilde{t}) \rangle_{\vec{x} \in \mathcal{R}}$ for an extruding cell i during $\tilde{t} = (t/\tau_0) \in [\tilde{t}_e - 2.5, \tilde{t}_e + 0.3125]$, where \tilde{t}_e denotes extrusion time and $\tau_0 = \xi R_0/\alpha$. The data shown in (c)-(d) correspond to all the considered parameters for cell-substrate (ω_{cw}) and relative cell-cell adhesions (Ω) and for four distinct realizations. Each gray line in the background represents an extruding cell, the red line shows the mean and the standard deviation of the normalized stresses.

normalized isotropic stress $\tilde{\sigma}^{\text{iso}}(\vec{x}) = \sigma^{\text{iso}}(\vec{x})/\sigma_{\text{max}}^{\text{iso}}$ and out-of-plane shear $\tilde{\sigma}_{xz}(\vec{x}) = \sigma_{xz}(\vec{x})/\sigma_{xz}^{\text{max}}$ where $\sigma_{\text{max}}^{\text{iso}}$

and σ_{xz}^{max} are the maximum values in their corresponding fields. (see Fig. 4(a)-(b)). We observe a high, out-

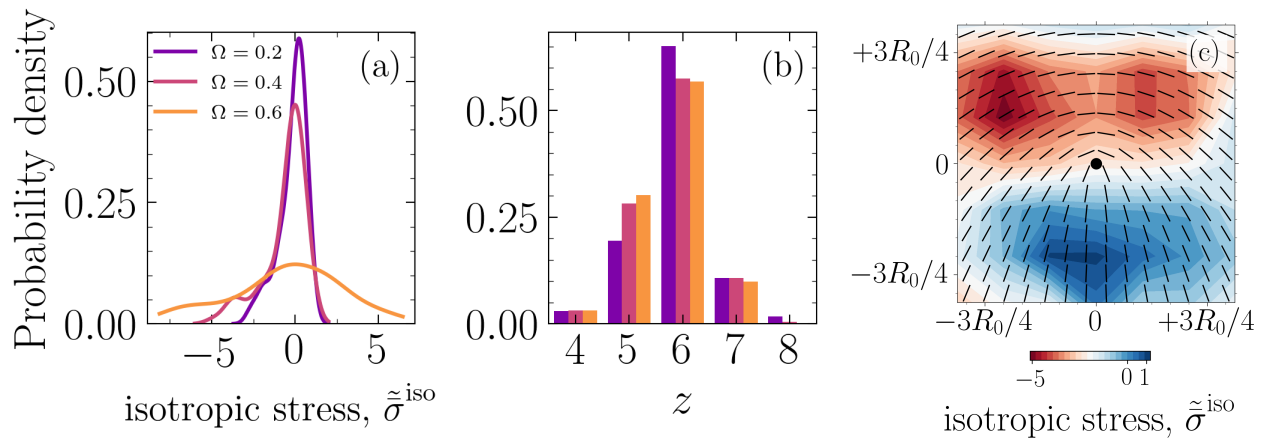


Figure 5. **Spatial localization of mechanical stress leading to extrusion events.** (a): Probability density function for the normalized, ensemble average of isotropic stress field, $\tilde{\sigma}^{\text{iso}}$, projected into xy -plane with $z = 0$ i.e. the basal side, around $+1/2$ defects for various cell-cell to cell-substrate adhesion ratios Ω (colors correspond to legend in (a)). (b): Probability density function for the number of neighbors z and various Ω , for all cells and simulation time steps. (c): normalized, ensemble average of isotropic stress field, $\tilde{\sigma}^{\text{iso}}(\vec{x}) = \bar{\sigma}^{\text{iso}}(\vec{x}) / \bar{\sigma}_{\text{max}}^{\text{iso}}$, with $\bar{\sigma}^{\text{iso}}$ representing the average field during defect life time, for nucleated defects, and $\bar{\sigma}_{\text{max}}^{\text{iso}}$ is the maximum of the average field, for the case $\omega_{\text{cw}} = 0.0025$ and $\Omega = 0.4$.

of-plane, shear stress concentration (Fig. 4(b)) as well as tensile and compressive stress pathways (Fig. 4(a)) reminiscent of force chains in granular systems [55].

Figure 4(c) shows the evolution of spatially averaged normalized isotropic stress for extruding cell i , $\bar{\sigma}_i^{\text{iso}}(\tilde{t}) = \langle \sigma^{\text{iso}}(\vec{x}, \tilde{t}) \rangle_{\vec{x} \in \mathcal{R}_i} / \langle \sigma^{\text{iso}}(\vec{x}, \tilde{t}) \rangle_{\vec{x} \in \mathcal{R}}$, demonstrating a clear stress build up, followed by a drop near $\tilde{t} - \tilde{t}_e = 0$, as a cell detaches the substrate and loses contact with other cells, where \tilde{t}_e is detected by our stress-independent criterion, $\mathcal{R} = \bigcup_{i=1}^N \mathcal{R}_i$ and \mathcal{R}_i is the domain associated with cell i , $\mathcal{R}_i := \{\vec{x} | \phi_i(\vec{x}) \geq 0.5\}$.

Similarly, Fig. 4(d) displays the spatially averaged normalized out-of-plane shear stress, $\bar{\sigma}_{xz}^i(\tilde{t}) = \langle \sigma_{xz}(\vec{x}, \tilde{t}) \rangle_{\vec{x} \in \mathcal{R}_i} / \langle \sigma_{xz}(\vec{x}, \tilde{t}) \rangle_{\vec{x} \in \mathcal{R}}$ prior to a cell extrusion and for all extrusion events in our simulations, i.e. nine cases and four realizations for each case. The shear stress prior to extrusion exhibits oscillations with large magnitudes relative to the mean field, a stark departure from their non-extruding counterparts (see Fig. 9 in SI). This may indicate a hindrance to cell movement as we explore further next.

Interestingly, the association of cell extrusion events with regions of high out-of-plane shear stress has parallels with the phenomenon of *plithotaxis*, where it was shown that cells collectively migrate along the orientation of the minimal in-plane intercellular shear stress [56]. In this context, based on the association of cell extrusion events with regions of high out-of-plane shear stress, we conjecture that high shear stress concentration hinders collective cell migration with cell extrusion providing a mechanism to re-establish the status-quo. This is also consistent with the observation we made earlier about large oscillations in $\bar{\sigma}_{xz}^i$ prior to an extrusion event, for

all extruding cells (Fig. 4(d)).

Shifting tendencies towards extrusion at nematic and hexatic disclinations

The results so far clearly demonstrate the existence of mechanical routes for cell removal that are associated with nematic and hexatic disclinations and are governed by the in-plane and out-of-plane mechanical stress patterns in the cell assembly. The relative strength of cell-cell to cell-substrate adhesion, Ω , further alter the likelihood of an extrusion event being associated with a $+1/2$ defect or a five-fold disclination. This is clearly observed in Fig. 2(d), that show the first moment of the distribution for $\tilde{d}_{\text{min}}^{+1/2}$, $m = \langle \tilde{d}_{\text{min}}^{+1/2} \rangle$, increases with $\Omega = \omega_{\text{cc}} / \omega_{\text{cw}}$ (see inset) while the peak of the probability density decreases with increasing Ω . At the same time, the probability of an extrusion occurring at a five-fold disclination increases with increasing Ω , as displayed in Fig. 2(e). However, nematic and hexatic order parameters do not show any clear trends with Ω (see Fig. 15 in SI). To better understand this tendency, we characterize the average isotropic stress fields around a $+1/2$ defect. This involves tracking each $+1/2$ defect starting from its nucleation and mapping the isotropic stress field, for each time step during the defect's life time, in a square domain of size $L \approx 1.5R_0$ centered on the defect location and accounting for its orientation, where L is chosen based on the peak in $\tilde{d}_{\text{min}}^{+1/2}$ (see Fig. 2(d)). An example for the normalized average isotropic stress field corresponding to $\omega_{\text{cw}} = 0.0025$ and $\Omega = 0.4$ is shown in Fig. 5(c), where $\tilde{\sigma}^{\text{iso}}(\vec{x}) = \bar{\sigma}^{\text{iso}}(\vec{x}) / \bar{\sigma}_{\text{max}}^{\text{iso}}$, with $\bar{\sigma}^{\text{iso}}$ representing the average field during defect life time, for all nucleated defects,

and $\bar{\sigma}_{\max}^{\text{iso}}$ is the maximum of the average field. This is in agreement with experimental measurements on epithelial monolayers [9, 19], with a compressive stress region near the head of the defect and a tensile region near the tail. Interestingly, there is an asymmetry in the intensity of stress in the compressive region at the head of the comet as opposed to the tensile region at the tail ($\approx 5\times$ higher). To expand on this observation, we focus on the probability density function for $\bar{\sigma}^{\text{iso}}$ and various Ω . Remarkably, as shown in Fig. 5(a), with increasing Ω , the peak of the probability density function decreases and the shoulders become wider, i.e. the stress localization becomes more spread. At the same time, it is worth noting that the probability for the occurrence of a five-fold disclination increases as Ω is increased, as shown in Fig. 5(b), while no clear trend is observed for the density of half-integer defects (see Fig. 11 in SI). Therefore, the more spread localized stress is more likely to only clear the lower energetic barrier associated with buckling of a five-fold disclination [51, 52] - forming a positive Gaussian curvature - as opposed to cells with six neighbors. Furthermore for a single disclination, this energy is higher for a seven-fold disclination [57] and in our case the rigid substrate defies any attempts by a seven-fold disclination to buckle and form a negative Gaussian curvature. Together, these results provide a potential explanation for why as Ω is increased, cells collectively have a tendency towards leveraging five-fold disclinations instead of $+1/2$ defects for extruding an unwanted cell.

Furthermore, one may naively think that only the distance between a half-integer nematic defect and an extrusion site is of importance. Such a view implicitly assumes the statistics we have presented (e.g. $\tilde{d}_{\min}^{\pm 1/2}$, $\tilde{\sigma}^{\text{iso}}$) correspond to independent events, disregarding the highly heterogeneous nature of such a complex, active system. This heterogeneous nature manifests in stress fields, as shown in Figs. 5(a) and 5(c) for the normalized ensemble average around a $+1/2$ defect. Therefore, the distance between a defect and an extrusion site, the intensity and the extent of the stress fields around that defect all play a role and are embedded in the statistics that we present in this work. In the future, it can be illuminating to study the effect of heterogeneity in the apical-basal mechanical response due to different mechanical properties and/or the nature of activity.

CONCLUSIONS

Our study presents a three-dimensional model of the collective migration-mediated cell elimination. Importantly, this framework allows for cell-substrate and cell-cell adhesion forces to be tuned independently. Our findings indeed suggest that varying the relative strength of cell-cell and cell-substrate adhesion can allow cells to switch between distinct mechanical pathways - leverag-

ing defects in nematic and hexatic phases - to eliminate unwanted cells through: (i) cell extrusion at $\pm 1/2$ topological defects in the cell orientation field, consistent with experimental observations [19]; and (ii) cell extrusion at five-fold disclinations in cell arrangement, where our results show a direct role of these disclinations in extruding the cells. Focusing on the extruded cells, the results demonstrate that increasing relative cell-cell adhesion increases the probability of an extruded cell being a five-fold disclination while weakening the correlation with $+1/2$ topological defects. This seems to emerge with a confluence of factors at play: (i) higher likelihood for a cell to be a five-fold disclination as $\Omega = \omega_{cc}/\omega_{cw}$ is increased, (ii) more spread stress concentration around a $+1/2$ defect with increasing Ω and (iii) a higher likelihood for such a diffused local stress field to only reach the lower energy barrier associated with buckling a five-fold disclination (forming a positive Gaussian curvature) as opposed to cells with six neighbors as well as seven-fold disclinations. In the latter case, in addition to higher energy barrier, the rigid substrate denies a seven-fold disclination to create any negative Gaussian curvatures.

Additionally, the presented framework provides access to the local stress field, including the out-of-plane shear components. Access to this information led us to conjecture that high shear stress concentration frustrates collective cell migration with cell extrusion providing a pathway to re-establish the status-quo. We expect these results to trigger further experimental studies of the mechanical routes to live cell elimination and probing the impact of tuning cell-cell and cell-substrate interactions, for example by molecular perturbations of E-cadherin adhesion complexes between the cells and/or focal adhesion between cells and substrate, as performed recently in the context of topological defect motion in cell monolayers [9]. In this study, we intentionally narrowed our focus to the interplay of cell-cell and cell-substrate adhesion, without accounting for cell proliferation. In its absence, simulations with high extrusion events may lose confluency. However, the identified mechanical routes to extrusion prevail in cases with both high and low number of extrusions, where confluency is maintained.

Finally, we anticipate that this modeling framework opens the door to several interesting and unresolved problems in studying three-dimensional features of cell layers. In particular, the mechanics can be coupled with biochemistry to study a wider range of mechanisms that affect live cell elimination. Additionally, using our framework the substrate rigidity can be relaxed in the future studies to further disentangle the impacts of cell-substrate adhesion from substrate deformation due to cell generated forces. Similarly three-dimensional geometries, such as spheroids or cysts can be examined. The links between collective cell migration and granular physics, in terms of force chains and liquid-to-solid transition, as well as probing the impact

of three-dimensionality and out-of-plane deformations on these processes, are exciting directions for future studies. Lastly, the co-existence of nematic and hexatic phases, their potential interactions and their interplay with curved surfaces are promising avenues for extending the work presented here.

MATERIALS AND METHODS

We consider a cellular monolayer consisting of $N = 400$ cells on a substrate with its surface normal $\vec{e}_n (= \vec{e}_z) = \vec{e}_x \times \vec{e}_y$ and periodic boundaries in both \vec{e}_x and \vec{e}_y , where $(\vec{e}_x, \vec{e}_y, \vec{e}_z)$ constitute the global orthonormal basis (Fig. 1). Cells are initiated on a two-dimensional simple cubic lattice and inside a cuboid of size $L_x = L_y = 320$, $L_z = 64$, grid size $a_0 = 1$ and with radius $R_0 = 8$. The cell-cell and cell-substrate interactions have contributions from both adhesion and repulsion, in addition to self-propulsion forces associated with cell polarity. To this end, each cell i is modeled as an active deformable droplet in three-dimensions using a phase-field, $\phi_i = \phi_i(\vec{x})$. The interior and exterior of cell i corresponds to $\phi_i = 1$ and $\phi_i = 0$, respectively, with a diffuse interface of length λ connecting the two regions and the midpoint, $\phi_i = 0.5$, delineating the cell boundary. A three-dimensional extension of the 2D free energy functional [37, 58–60] is considered with additional contributions to account for cell-cell and cell-substrate adhesions:

$$\begin{aligned} \mathcal{F} = & \sum_i^N \frac{\gamma}{\lambda} \int d\vec{x} \{ 4\phi_i^2 (1 - \phi_i)^2 + \lambda^2 (\vec{\nabla}\phi_i)^2 \} \\ & + \sum_i^N \mu \left(1 - \frac{1}{V_0} \int d\vec{x} \phi_i^2 \right)^2 + \sum_i^N \sum_{j \neq i} \frac{\kappa_{cc}}{\lambda} \int d\vec{x} \phi_i^2 \phi_j^2 \\ & + \sum_i^N \sum_{j \neq i} \frac{\omega_{cc}}{\lambda^2} \int d\vec{x} \vec{\nabla}\phi_i \cdot \vec{\nabla}\phi_j + \sum_i^N \frac{\kappa_{cw}}{\lambda} \int d\vec{x} \phi_i^2 \phi_w^2 \\ & + \sum_i^N \frac{\omega_{cw}}{\lambda^2} \int d\vec{x} \vec{\nabla}\phi_i \cdot \vec{\nabla}\phi_w, \end{aligned} \quad (1)$$

where \mathcal{F} contains a contribution due to the Cahn-Hilliard free energy [61] which stabilizes the cell interface, followed by a soft constraint for cell volume around $V_0 (= (4/3)\pi R_0^3)$, such that cells - each initiated with radius R_0 - are compressible. Additionally, κ and ω capture repulsion and adhesion between cell-cell (subscript cc) and cell-substrate (subscript cw), respectively. Moreover γ sets the cell stiffness and μ captures cell compressibility and ϕ_w denotes a static phase-field representing the substrate. This approach resolves the cellular interfaces and provides access to intercellular forces. The dynamics for field ϕ_i can be defined as:

$$\partial_t \phi_i + \vec{v}_i \cdot \vec{\nabla} \phi_i = -\frac{\delta \mathcal{F}}{\delta \phi_i}, \quad i = 1, \dots, N, \quad (2)$$

where \mathcal{F} is defined in Eq. (1) and \vec{v}_i is the total velocity of cell i . To resolve the forces generated at the cellular interfaces, we consider the following over-damped dynamics for cells:

$$\vec{t}_i = \xi \vec{v}_i - \vec{F}_i^{\text{sp}} = \int d\vec{x} \phi_i \vec{\nabla} \cdot \mathbf{\Pi}^{\text{int}}, \quad (3)$$

where \vec{t}_i denotes traction as defined for Bayesian Inversion Stress Microscopy in [19], ξ is substrate friction and $\vec{F}_i^{\text{sp}} = \alpha \vec{p}_i$ represents self-propulsion forces due to polarity, constantly pushing the system out-of-equilibrium. In this vein, α characterizes the strength of polarity force and $\mathbf{\Pi}^{\text{int}} = (\sum_i -(\delta \mathcal{F} / \delta \phi_i)) \mathbf{1}$. While only passive interactions are considered here, active nematic interactions can be readily incorporated in this framework [9, 37]. To complete the model, the dynamics of front-rear cell polarity is introduced based on contact inhibition of locomotion (CIL) [62, 63] by aligning the polarity of the cell to the direction of the total interaction force acting on the cell [64, 65]. As such, the polarization dynamics is given by:

$$\partial_t \theta_i = -J |\vec{t}_i| \Delta \theta_i + D_r \eta, \quad (4)$$

where $\theta_i \in [-\pi, \pi]$ is the angle associated with polarity vector, $\vec{p}_i = (\cos \theta_i, \sin \theta_i, 0)$ and η is the Gaussian white noise with zero mean, unit variance, D_r is rotational diffusivity, $\Delta \theta_i$ is the angle between \vec{p}_i and \vec{t}_i , and positive constant J sets the alignment time scale. It is worth noting that the self-propulsion forces, \vec{F}_i^{sp} , associated with cell polarity, \vec{p}_i , acts in-plane but can induce out-of-plane components in force and velocity fields as a cell described by $\phi_i(\vec{x})$ deforms in three-dimensions (see Eq.(3)).

We perform large scale simulations with a focus on the interplay of cell-cell and cell-substrate adhesion strengths and its impact on cell expulsion from the monolayer. To this end, we set the cell-substrate adhesion strength $\omega_{cw} \in \{0.0015, 0.002, 0.0025\}$ and vary the cell-substrate to cell-cell adhesion ratio in the range $\Omega = \omega_{cc} / \omega_{cw} \in \{0.2, 0.4, 0.6\}$. For each case in this study (total of nine), we simulate four distinct realizations with a total of $n_{\text{sim}} = 29,000$ time steps. All results are reported in dimensionless units, introduced throughout the text, and the simulation parameters are chosen within the range that was previously shown to reproduce defect flow fields in epithelial layers [9] (see SI).

ACKNOWLEDGMENTS

S.M. is grateful for the generous support of the Rosenfeld Foundation fellowship at the Niels Bohr Institute, University of Copenhagen. S.M., G.R. and J.A. acknowledge support for this research provided by US ARO funding through the Multidisciplinary University Research Initiative (MURI) Grant No. W911NF-19-1-0245. A. D.

acknowledges funding from the Novo Nordisk Foundation (grant No. NNF18SA0035142 and NERD grant No. NNF21OC0068687), Villum Fonden Grant no. 29476, and the European Union via the ERC-Starting Grant PhysCoMeT. The authors would like to thank Dr. Lakshmi Balasubramaniam and Prof. Benoît Ladoux (Institut Jacques Monod, University Paris City), Guanming Zhang and Prof. Julia M. Yeomans (The Rudolf Peierls Centre for Theoretical Physics, University of Oxford), Prof. Jörn Dunkel (Mathematics Department, MIT) and Prof. M. Cristina Marchetti (Department of Physics, University of California Santa Barbara) for helpful discussions. The authors are also grateful for the comments and the feedback provided by the anonymous reviewers.

-
- [1] K. Chiou and E.-M. S. Collins, Why we need mechanics to understand animal regeneration, *Developmental Biology* **433**, 155 (2018).
- [2] F. Vafa and L. Mahadevan, Active nematic defects and epithelial morphogenesis, *Physical Review Letters* **129**, 10.1103/physrevlett.129.098102 (2022).
- [3] E. H. Barriga, K. Franze, G. Charras, and R. Mayor, Tissue stiffening coordinates morphogenesis by triggering collective cell migration in vivo, *Nature* **554**, 523 (2018).
- [4] A. Brugués, E. Anon, V. Conte, J. H. Veldhuis, M. Gupta, J. Colombelli, J. J. Muñoz, G. W. Brodland, B. Ladoux, and X. Trepat, Forces driving epithelial wound healing, *Nature Physics* **10**, 683 (2014).
- [5] C. D. Pascalis and S. Etienne-Manneville, Single and collective cell migration: The mechanics of adhesions, *Molecular Biology of the Cell* **28**, 1833 (2017).
- [6] S. A. Maskarinec, C. Franck, D. A. Tirrell, and G. Ravichandran, Quantifying cellular traction forces in three dimensions, *Proceedings of the National Academy of Sciences* **106**, 22108 (2009).
- [7] B. Ladoux, Cells guided on their journey, *Nature Physics* **5**, 377 (2009).
- [8] B. Ladoux and R.-M. Mège, Mechanobiology of collective cell behaviours, *Nature Reviews Molecular Cell Biology* **18**, 743 (2017).
- [9] L. Balasubramaniam, A. Doostmohammadi, T. B. Saw, G. H. N. S. Narayana, R. Mueller, T. Dang, M. Thomas, S. Gupta, S. Sonam, A. S. Yap, Y. Toyama, R.-M. Mège, J. M. Yeomans, and B. Ladoux, Investigating the nature of active forces in tissues reveals how contractile cells can form extensile monolayers, *Nature Materials* 10.1038/s41563-021-00919-2 (2021).
- [10] J. Rosenblatt, M. C. Raff, and L. P. Cramer, An epithelial cell destined for apoptosis signals its neighbors to extrude it by an actin- and myosin-dependent mechanism, *Current Biology* **11**, 1847 (2001).
- [11] C. Hogan, S. Dupré-Crochet, M. Norman, M. Kajita, C. Zimmermann, A. E. Pelling, E. Piddini, L. A. Baena-López, J.-P. Vincent, Y. Itoh, H. Hosoya, F. Pichaud, and Y. Fujita, Characterization of the interface between normal and transformed epithelial cells, *Nature Cell Biology* **11**, 460 (2009).
- [12] E. Marinari, A. Mehonic, S. Curran, J. Gale, T. Duke, and B. Baum, Live-cell delamination counterbalances epithelial growth to limit tissue overcrowding, *Nature* **484**, 542 (2012).
- [13] G. T. Eisenhoffer, P. D. Loftus, M. Yoshigi, H. Otsuna, C.-B. Chien, P. A. Morcos, and J. Rosenblatt, Crowding induces live cell extrusion to maintain homeostatic cell numbers in epithelia, *Nature* **484**, 546 (2012).
- [14] R. Levayer, C. Dupont, and E. Moreno, Tissue crowding induces caspase-dependent competition for space, *Current Biology* **26**, 670 (2016).
- [15] V. K. Dwivedi, C. Pardo-Pastor, R. Droste, J. N. Kong, N. Tucker, D. P. Denning, J. Rosenblatt, and H. R. Horvitz, Replication stress promotes cell elimination by extrusion, *Nature* **593**, 591 (2021).
- [16] Y. Toyama, X. G. Peralta, A. R. Wells, D. P. Kiehart, and G. S. Edwards, Apoptotic force and tissue dynamics during drosophila embryogenesis, *Science* **321**, 1683 (2008).
- [17] A. P. Le, J.-F. Rupperecht, R.-M. Mège, Y. Toyama, C. T. Lim, and B. Ladoux, Adhesion-mediated heterogeneous actin organization governs apoptotic cell extrusion, *Nature Communications* **12**, 10.1038/s41467-020-20563-9 (2021).
- [18] G. M. Slatum and J. Rosenblatt, Tumour cell invasion: an emerging role for basal epithelial cell extrusion, *Nature Reviews Cancer* **14**, 495 (2014).
- [19] T. B. Saw, A. Doostmohammadi, V. Nier, L. Kocgozlu, S. Thampi, Y. Toyama, P. Marq, C. T. Lim, J. M. Yeomans, and B. Ladoux, Topological defects in epithelia govern cell death and extrusion, *Nature* **544**, 212 (2017).
- [20] K. Kawaguchi, R. Kageyama, and M. Sano, Topological defects control collective dynamics in neural progenitor cell cultures, *Nature* **545**, 327 (2017).
- [21] G. Duclos, C. Blanch-Mercader, V. Yashunsky, G. Salbreux, J.-F. Joanny, J. Prost, and P. Silberzan, Spontaneous shear flow in confined cellular nematics, *Nature Physics* **14**, 728 (2018).
- [22] C. Blanch-Mercader, V. Yashunsky, S. Garcia, G. Duclos, L. Giomi, and P. Silberzan, Turbulent dynamics of epithelial cell cultures, *Physical Review Letters* **120**, 10.1103/physrevlett.120.208101 (2018).
- [23] T. H. Tan, J. Liu, P. W. Miller, M. Tekant, J. Dunkel, and N. Fakhri, Topological turbulence in the membrane of a living cell, *Nature Physics* **16**, 657 (2020).
- [24] J. Zhang, N. Yang, P. K. Kreeger, and J. Notbohm, Topological defects in the mesothelium suppress ovarian cancer cell clearance, *APL Bioengineering* **5**, 036103 (2021).
- [25] A.-K. Classen, K. I. Anderson, E. Marois, and S. Eaton, Hexagonal packing of drosophila wing epithelial cells by the planar cell polarity pathway, *Developmental Cell* **9**, 805 (2005).
- [26] K. Sugimura and S. Ishihara, The mechanical anisotropy in a tissue promotes ordering in hexagonal cell packing, *Development* **140**, 4091 (2013).
- [27] A. Pasupalak, L. Yan-Wei, R. Ni, and M. P. Ciamarra, Hexatic phase in a model of active biological tissues, *Soft Matter* **16**, 3914 (2020).
- [28] A. Maitra, M. Lenz, and R. Voituriez, Chiral active hexatics: Giant number fluctuations, waves, and destruction of order, *Physical Review Letters* **125**, 10.1103/physrevlett.125.238005 (2020).
- [29] L. A. Hoffmann, L. N. Carenza, J. Eckert, and L. Giomi, Theory of defect-mediated morphogenesis, *Science Ad-*

- vances **8**, 10.1126/sciadv.abk2712 (2022).
- [30] J.-M. Armengol-Collado, L. N. Carenza, J. Eckert, D. Krommydas, and L. Giomi, Epithelia are multiscale active liquid crystals, *bioRxiv* 10.1101/2022.02.01.478692 (2022).
- [31] B. Loewe, M. Chiang, D. Marenduzzo, and M. C. Marchetti, Solid-liquid transition of deformable and overlapping active particles, *Physical Review Letters* **125**, 10.1103/physrevlett.125.038003 (2020).
- [32] J. Rozman, M. Krajnc, and P. Zihlerl, Collective cell mechanics of epithelial shells with organoid-like morphologies, *Nature Communications* **11**, 10.1038/s41467-020-17535-4 (2020).
- [33] J. Rozman, M. Krajnc, and P. Zihlerl, Morphologies of compressed active epithelial monolayers, *The European Physical Journal E* **44**, 10.1140/epje/s10189-021-00094-x (2021).
- [34] A. Doostmohammadi, S. P. Thampi, T. B. Saw, C. T. Lim, B. Ladoux, and J. M. Yeomans, Celebrating soft matter's 10th anniversary: Cell division: a source of active stress in cellular monolayers, *Soft Matter* **11**, 7328 (2015).
- [35] A. Doostmohammadi, S. P. Thampi, and J. M. Yeomans, Defect-mediated morphologies in growing cell colonies, *Physical Review Letters* **117**, 10.1103/physrevlett.117.048102 (2016).
- [36] P. G. de Gennes and J. Prost, *The physics of liquid crystals*, 2nd ed., The international series of monographs on physics No. 83 (Clarendon Press, Oxford, 1998) oCLC: 833446379.
- [37] R. Mueller, J. M. Yeomans, and A. Doostmohammadi, Emergence of active nematic behavior in monolayers of isotropic cells, *Physical Review Letters* **122**, 10.1103/physrevlett.122.048004 (2019).
- [38] D. Wenzel and A. Voigt, Multiphase field models for collective cell migration, *Physical Review E* **104**, 10.1103/physreve.104.054410 (2021).
- [39] M. Bär, R. Großmann, S. Heidenreich, and F. Peruani, Self-propelled rods: Insights and perspectives for active matter, *Annual Review of Condensed Matter Physics* **11**, 441 (2020).
- [40] O. J. Meacock, A. Doostmohammadi, K. R. Foster, J. M. Yeomans, and W. M. Durham, Bacteria solve the problem of crowding by moving slowly, *Nature Physics* **17**, 205 (2020).
- [41] A. Amiri, R. Mueller, and A. Doostmohammadi, Unifying polar and nematic active matter: emergence and co-existence of half-integer and full-integer topological defects, *Journal of Physics A: Mathematical and Theoretical* **55**, 094002 (2022).
- [42] S. Kaliman, M. Hubert, C. Wollnik, L. Nuić, D. Vurnek, S. Gehrler, J. Lovrić, D. Dudziak, F. Rehfeldt, and A.-S. Smith, Mechanical regulation of epithelial tissue homeostasis, *Physical Review X* **11**, 10.1103/physrevx.11.031029 (2021).
- [43] P. Gómez-Gálvez, P. Vicente-Munuera, A. Tagua, C. Forja, A. M. Castro, M. Letrán, A. Valencia-Expósito, C. Grima, M. Bermúdez-Gallardo, Ó. Serrano-Pérez-Higueras, F. Cavodeassi, S. Sotillos, M. D. Martín-Bermudo, A. Márquez, J. Buceta, and L. M. Escudero, Scutoids are a geometrical solution to three-dimensional packing of epithelia, *Nature Communications* **9**, 10.1038/s41467-018-05376-1 (2018).
- [44] F. T. Lewis, The correlation between cell division and the shapes and sizes of prismatic cells in the epidermis of cucumis, *The Anatomical Record* **38**, 341 (1928).
- [45] M. Kokic, A. Iannini, G. Villa-Fombuena, F. Casares, and D. Iber, Minimisation of surface energy drives apical epithelial organisation and gives rise to lewis law, *bioRxiv* 10.1101/590729 (2019).
- [46] S. Kim, M. Cai, and S. Hilgenfeldt, Lewis' law revisited: the role of anisotropy in size-topology correlations, *New Journal of Physics* **16**, 015024 (2014).
- [47] D. Wenzel, S. Praetorius, and A. Voigt, Topological and geometrical quantities in active cellular structures, *The Journal of Chemical Physics* **150**, 164108 (2019).
- [48] S. Okuda and K. Fujimoto, A Mechanical Instability in Planar Epithelial Monolayers Leads to Cell Extrusion, *Biophysical Journal* **118**, 2549 (2020).
- [49] W. T. M. Irvine, V. Vitelli, and P. M. Chaikin, Pleats in crystals on curved surfaces, *Nature* **468**, 947 (2010).
- [50] L. D. Landau, E. M. Lifšic, and L. D. Landau, *Theory of elasticity*, 2nd ed., *Course of theoretical physics / by L. D. Landau and E. M. Lifshitz No. Vol. 7* (Pergamon Press, Oxford, 1986).
- [51] H. S. Seung and D. R. Nelson, Defects in flexible membranes with crystalline order, *Physical Review A* **38**, 1005 (1988).
- [52] E. Guitter and M. Kardar, Tethering, crumpling, and melting transitions in hexatic membranes, *Europhysics Letters (EPL)* **13**, 441 (1990).
- [53] J. Christoffersen, M. M. Mehrabadi, and S. Nemat-Nasser, A micromechanical description of granular material behavior, *Journal of Applied Mechanics* **48**, 339 (1981).
- [54] H. Li, D. Matsunaga, T. S. Matsui, H. Aosaki, G. Kinoshita, K. Inoue, A. Doostmohammadi, and S. Deguchi, Wrinkle force microscopy: a machine learning based approach to predict cell mechanics from images, *Communications Biology* **5**, 10.1038/s42003-022-03288-x (2022).
- [55] T. S. Majmudar and R. P. Behringer, Contact force measurements and stress-induced anisotropy in granular materials, *Nature* **435**, 1079 (2005).
- [56] D. T. Tambe, C. C. Hardin, T. E. Angelini, K. Rajendran, C. Y. Park, X. Serra-Picamal, E. H. Zhou, M. H. Zaman, J. P. Butler, D. A. Weitz, J. J. Fredberg, and X. Trepat, Collective cell guidance by cooperative intercellular forces, *Nature Materials* **10**, 469 (2011).
- [57] M. W. Deem and D. R. Nelson, Free energies of isolated five- and sevenfold disclinations in hexatic membranes, *Physical Review E* **53**, 2551 (1996).
- [58] B. Palmieri, Y. Bresler, D. Wirtz, and M. Grant, Multiple scale model for cell migration in monolayers: Elastic mismatch between cells enhances motility, *Sci. Rep.* **5**, 11745 (2015).
- [59] I. S. Aranson, ed., *Physical models of cell motility*, 1st ed., *Biological and Medical Physics, Biomedical Engineering* (Springer International Publishing, Basel, Switzerland, 2015).
- [60] B. A. Camley and W.-J. Rappel, Physical models of collective cell motility: from cell to tissue, *Journal of Physics D: Applied Physics* **50**, 113002 (2017).
- [61] J. W. Cahn and J. E. Hilliard, Free energy of a nonuniform system. I. interfacial free energy, *Journal of Chemical Physics* **28**, 258 (1958).
- [62] M. Abercrombie and J. E. Heaysman, Observations on the social behaviour of cells in tissue culture, *Experimen-*

- tal Cell Research **6**, 293 (1954).
- [63] M. Abercrombie, Contact inhibition and malignancy, *Nature* **281**, 259 (1979).
- [64] B. Smeets, R. Alert, J. Pešek, I. Pagonabarraga, H. Ramon, and R. Vincent, Emergent structures and dynamics of cell colonies by contact inhibition of locomotion, *Proceedings of the National Academy of Sciences* **113**, 14621 (2016).
- [65] G. Peyret, R. Mueller, J. d’Alessandro, S. Begnaud, P. Marcq, R.-M. Mège, J. M. Yeomans, A. Doostmohammadi, and B. Ladoux, Sustained oscillations of epithelial cell sheets, *Biophysical Journal* **117**, 464 (2019).
- [66] D. R. Nelson and B. I. Halperin, Dislocation-mediated melting in two dimensions, *Physical Review B* **19**, 2457 (1979).

KOLMOGOROV-SMIRNOV TEST FOR CORRELATION BETWEEN EXTRUSION EVENTS AND NEMATIC DEFECTS

We use a hypothesis-testing approach to explore the existence of a correlation between the extrusion events in our simulations and nucleation of nematic topological defects. Specifically, we hypothesize that the extrusion events are uncorrelated with the topological defects. To falsify this, we use a poisson point process to randomly generate extrusion events and quantify the minimum distance, $\bar{d}_{\min} = d_{\min}/R_0$ between the extrusion location and the nearest half-integer topological defects. To this end, for each simulation, we generate five realization of extrusion events using a poisson point process with intensity set equal to the number of extrusions in that particular simulation. Furthermore, we assign an extrusion time, t_e , using a uniform distribution $t_e \sim U(1, n_{\text{sim}})$. Then, we quantify the minimum distance \bar{d}_{\min} as we have done for our simulations. The results are shown in Fig. 6. To falsify the stated hypothesis, we use a Kolmogorov-Smirnov (KS) test to measure if the two samples, one based in our simulations and one based on randomly generated extrusion events, belong to the same distribution. As shown in Table I, the results of the KS test falsifies this hypothesis, i.e. simulation based extrusion events are uncorrelated with the topological defects.

SIMULATION PARAMETERS

We perform large scale simulations with a focus on the interplay of cell-cell and cell-substrate adhesion strengths on collective cell migration and its impact on cell expulsion from the monolayer. Following [37], the space and time discretization in our simulations are based on the average radius of MDCK cells, $\sim 5\mu m$, velocity $\sim 20\mu m/h$ and average pressure of $\sim 100Pa$, measured experimentally in MDCK monolayers [19], corresponding to $\Delta x \sim 0.5\mu m$, $\Delta t \sim 0.1s$ and $\Delta F \sim 1.5nN$ for force. In this study, we set the cell-substrate adhesion strength $\omega_{cw} \in \{0.0015, 0.002, 0.0025\}$ and vary the cell-substrate to cell-cell adhesion ratio in the range $\Omega = \omega_{cc}/\omega_{cw} \in \{0.2, 0.4, 0.6\}$. Based on previous experimental and theoretical studies [9, 37, 65], the other simulation parameters are $\kappa_{cc} = 0.5$, $\kappa_{cw} = 0.15$, $\xi = 1$, $\alpha = 0.05$, $\lambda = 3$, $\mu = 45$, $D_r = 0.01$ and $J = 0.005$, unless stated otherwise.

LEWIS'S EMPIRICAL RELATION

The empirical relationship proposed by F. Lewis [44] is generally valid for cellular matter that fill in the space without gaps. In our simulations, we can loose confluency due to cellular extrusions. Furthermore, even in the case of a confluent cellular layer, i.e. no gaps between cells, Lewis's law fails to capture the correlation between normalized area and number of neighbors (see [46, 47]). However, we still investigated the existence of such correlation in our simulations. To this end, we used the following linear and quadratic relationships [45]:

$$\frac{\bar{A}_z}{\bar{A}} = \frac{z - 2}{4} \quad (5)$$

$$\frac{\bar{A}_z}{\bar{A}} = \left(\frac{z}{6}\right)^2 \quad (6)$$

where \bar{A}_z is the average area of cells with z neighbors and \bar{A} is the average of area of the cells in the monolayer. As shown in Fig. 7, the agreement is poor. Furthermore, while the projected area of an extruding cell decreases prior to extrusion, the number of neighbors its interacting with remains generally unchanged. This is shown in Fig. 7.

COORDINATION NUMBER COMPUTATION

To compute the coordination number, we use interaction between the cells instead of voronoi tessellation.

This is because when confluency is lost and there is a heterogeneous density of cells on the substrate, voronoi tessellation would over-estimate a cell's number of neighbors. To this end, we consider two cells, i and j , as interacting cells if the following is satisfied:

$$\{\phi_i|\phi_i > 0.25\} \cap \{\phi_j|\phi_j > 0.25\} \neq \emptyset \quad (7)$$

OUT-OF-PLANE SHEAR, σ_{xz} , FOR NON-EXTRUDING CELLS

The fluctuations in out-of-plane shear, $\bar{\sigma}_{xz}^i(\bar{t}) = \langle \sigma_{xz}(\bar{x}, \bar{t}) \rangle_{\bar{x} \in \mathcal{R}_i} / \langle \sigma_{xz}(\bar{x}, \bar{t}) \rangle_{\bar{x} \in \mathcal{R}}$ for an extruding cell i normalized by the maximum out-of-plane shear for all non-extruding cells in the same temporal window, as shown in Fig. 9.

HALF-INTEGER DEFECT STATISTICS

We have computed the lifetime for a half-integer defect by tracking that defect from its nucleation to annihilation in our simulations. The probability density for defect lifetimes are shown in Fig. 10. Furthermore, we computed the defect density, which we define as the number of defects, either $+1/2$ or $-1/2$, detected at each simulation (time) frame divided by the domain of the simulation, $a = L_x \times L_y$. This is shown in Fig. 11. We also computed the distances between half-integer defects for each simulation (time) frame, as shown in Fig. 12. The peak in these probability densities are much larger than the peak of the minimum distance to $\pm 1/2$ defects, as shown in Fig. 2(c),(d).

PHASE-DIAGRAM FOR EXTRUSION INTENSITY

To further explore the impact of asymmetric interaction of the cells with apical and basal sides, we have performed additional simulations varying the strength of the cell-substrate interactions. Fig. 13 shows how changing cell-substrate adhesion (basal), ω_{cw} , affects the extrusion rate. The results show that increasing cell-substrate adhesion leads to less extrusion events, while the ratio $\Omega = \omega_{cc}/\omega_{cw}$ does not seem to play a significant role on the likelihood of an extrusion event occurring.

ENERGY SPECTRA

We calculated energy spectra for different cell-cell adhesion strengths, which suggests different power-law regimes, as shown in Fig. 14. The kinetic energy spectrum, $\hat{E}_v = \frac{1}{2} \langle \hat{v}_i(k) \hat{v}_i(k) \rangle$ where \hat{v}_i is the Fourier transforms of the velocity field, and $\tilde{E}_v = \hat{E}_v(k) / \hat{E}_v^{\max}(k)$. Furthermore, $\tilde{k} = k / (2\pi / R_0)$.

p -ATIC ORDER

We computed the p -atic order parameter, associated with a liquid crystal exhibiting p -fold rotational symmetry [66], $\psi_p^i = \frac{1}{N_n^i} \sum_j^{N_n^i} \exp(pi\theta_{ij})$ where N_n^i is the

number of neighbors for cell i , θ_{ij} is the angle between vector \vec{r}_{ij} , connecting cell i and neighboring cell j , and \vec{e}_x . Lastly, $p = 2$ for nematic and $p = 6$ for hexatic phases. The mean of the absolute value, $|\bar{\psi}_2|$ and $|\bar{\psi}_6|$ for various $\Omega = \omega_{cc} / \omega_{cw}$ is shown in Fig. 15.

EXAMPLE FOR EQUILIBRATED MONOLAYER CONFIGURATION

In absence of activity, cells tend to equilibrate into a hexagonal lattice. An example is shown in Fig. 16(a) along with the temporal evolution of the mean hexatic order parameter, $|\bar{\psi}_6|$ displayed in Fig. 16(b), plateauing at $|\bar{\psi}_6| = 1$ indicative of perfect hexatic order.

Table I. Results of the Kolmogorov-Smirnov (KS) tests for various cell-cell to cell-substrate adhesion ratio ($\Omega = \omega_{cc}/\omega_{cw}$) and for half-integer topological defects. Both statistics and p -value are KS test results and n corresponds to the number of samples in each distribution, for both simulations and the extrusion events generated through a poisson point process.

Probability density statistics	p -value	n (simulations)	n (randomly generated)
$\Omega = 0.2$ (+1/2)	0.8221	1.95×10^{-154}	426
$\Omega = 0.4$ (+1/2)	0.228	2.22×10^{-15}	648
$\Omega = 0.6$ (+1/2)	0.827	5.12×10^{-212}	551
$\Omega = 0.2$ (-1/2)	0.802	1.22×10^{-15}	426
$\Omega = 0.4$ (-1/2)	0.840	8.17×10^{-260}	648
$\Omega = 0.6$ (-1/2)	0.824	2.84×10^{-198}	551

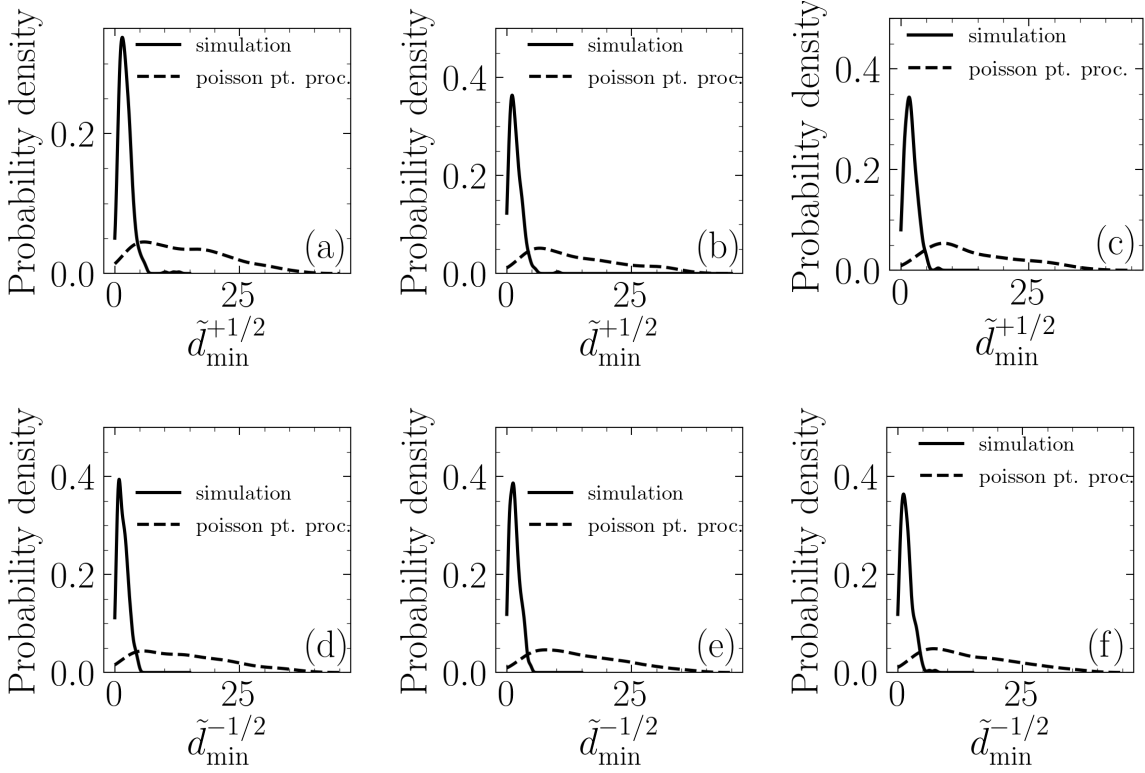


Figure 6. Probability density of the normalized minimum distance, $\tilde{d}_{\min}^{+1/2}$ between an extrusion event and the nearest +1/2 topological defect (a-c) for $\Omega = 0.2$ (a), $\Omega = 0.4$ (b) and $\Omega = 0.6$ (c). Probability density of the normalized minimum distance, $\tilde{d}_{\min}^{-1/2}$ between an extrusion event and the nearest -1/2 topological defect (d-f) for $\Omega = 0.2$ (d), $\Omega = 0.4$ (e) and $\Omega = 0.6$ (f).

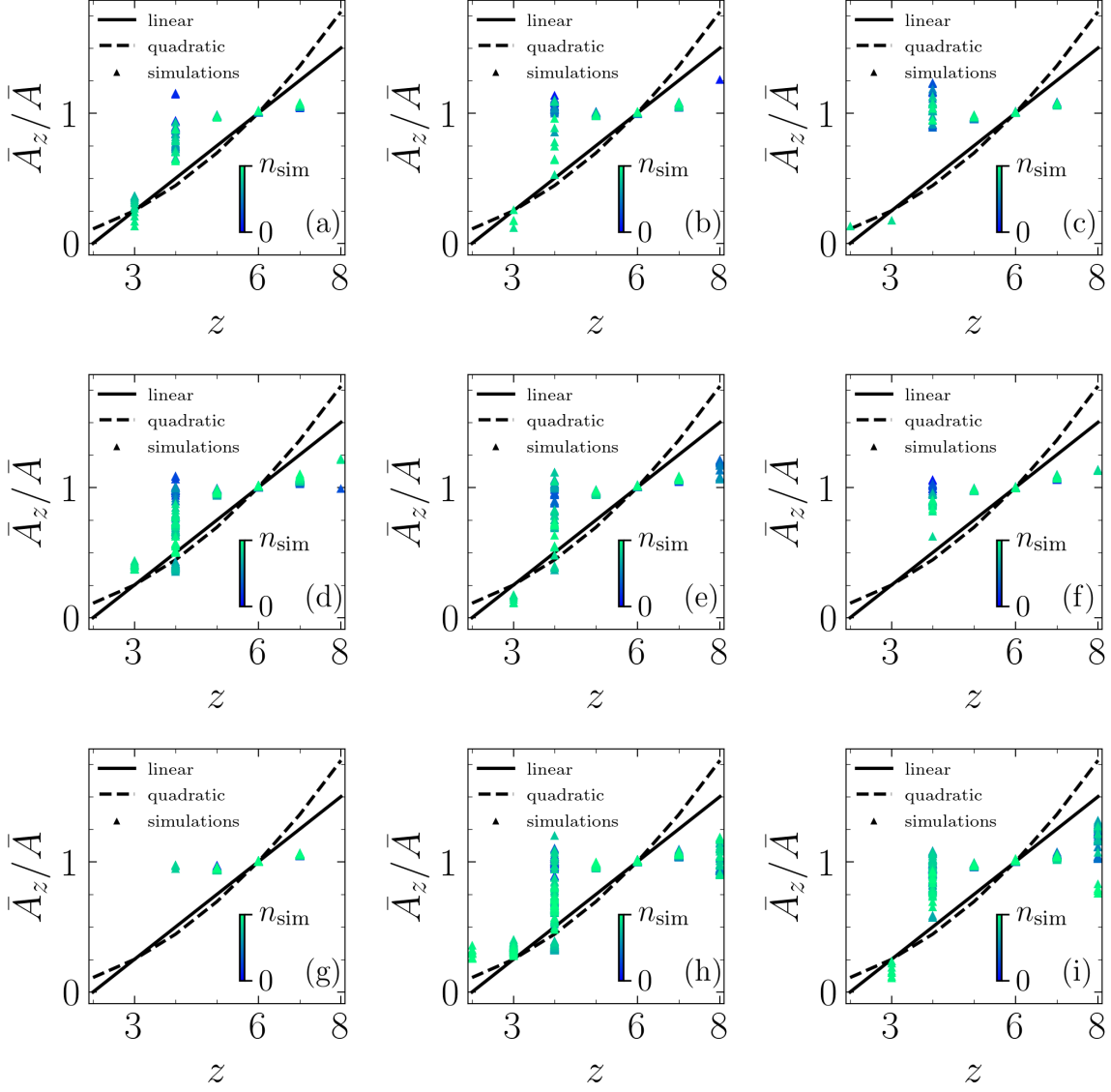


Figure 7. (a-i): Lewis's relationship compared with our simulations for $\omega_{cw} = 0.0015$ and $\Omega = 0.2$ (a), $\Omega = 0.4$ (b) and $\Omega = 0.6$ (c); $\omega_{cw} = 0.002$ and $\Omega = 0.2$ (d), $\Omega = 0.4$ (e) and $\Omega = 0.6$ (f) ; and $\omega_{cw} = 0.0025$ and $\Omega = 0.2$ (g), $\Omega = 0.4$ (h) and $\Omega = 0.6$ (i).

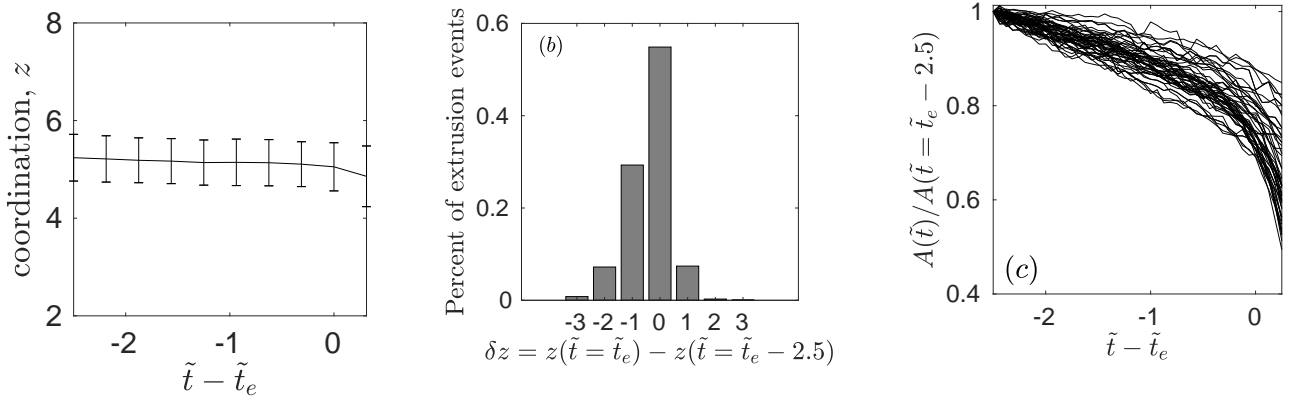


Figure 8. (a) The average and standard deviation of coordination number - number of interacting neighbors - for an extruding cell. The data corresponds to all simulations and the four distinct realizations considered in manuscript. (b) Percent of extrusion events with a given z - characterizing the change in number of interacting neighbors at extrusion time \tilde{t}_e and $\tilde{t}_e - 2.5$. The data corresponds to all simulations and the four distinct realizations considered in manuscript. (c) The temporal evolution of area for extruding cells normalized with the area at $\tilde{t}_e - 2.5$, for one of the realizations.

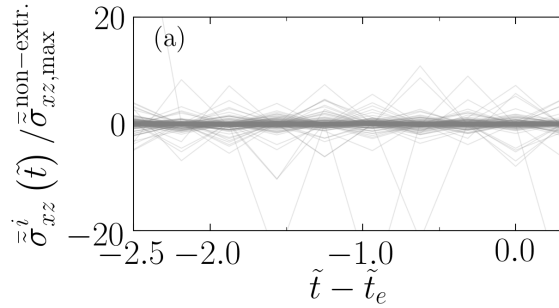


Figure 9. (a): Temporal evolution of the out-of-plane shear stress for an extruding cell i normalized by the maximum of the out-of-plane shear for all non-extruding cells within the same temporal window.

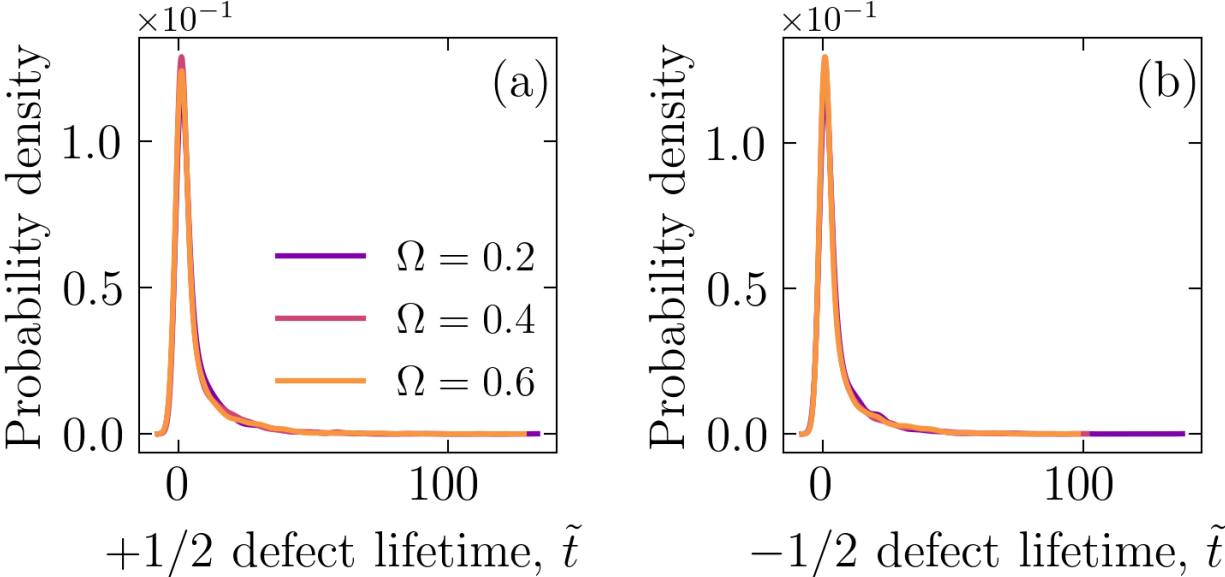


Figure 10. (a) The probability density of +1/2 and (b) -1/2 defect lifetimes.

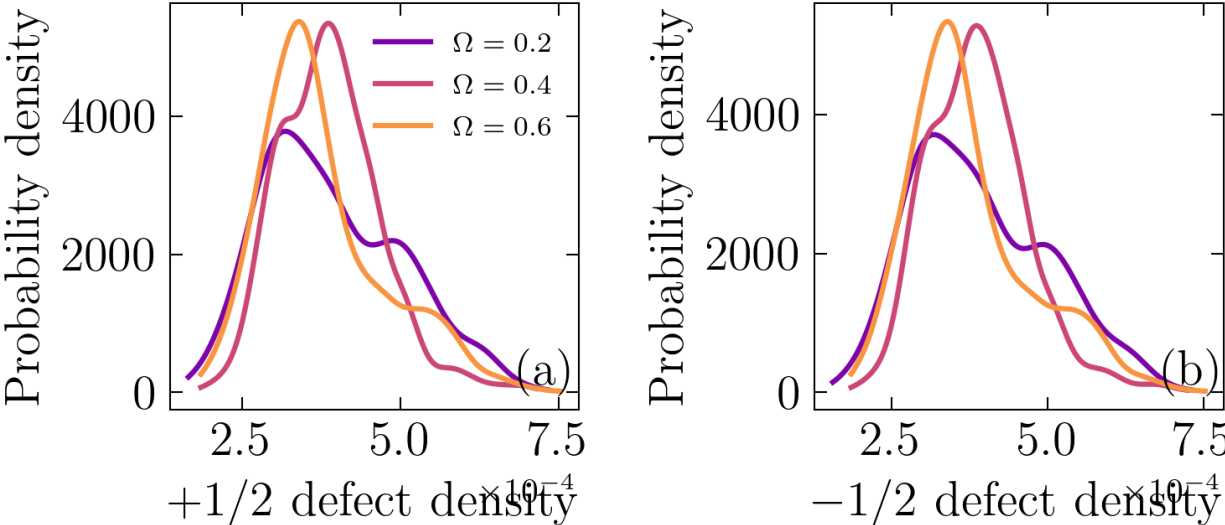


Figure 11. Probability density of (a) +1/2 and (b) -1/2 defect density distributions.

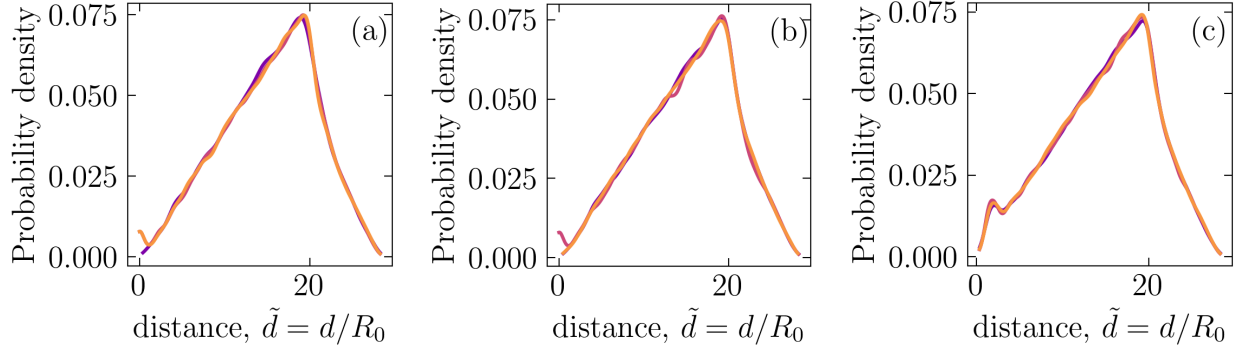


Figure 12. Probability density of pairwise distance between (a) $+1/2$ and $+1/2$ defects, (b) $-1/2$ and $-1/2$ defects and (c) $+1/2$ and $-1/2$ defects.

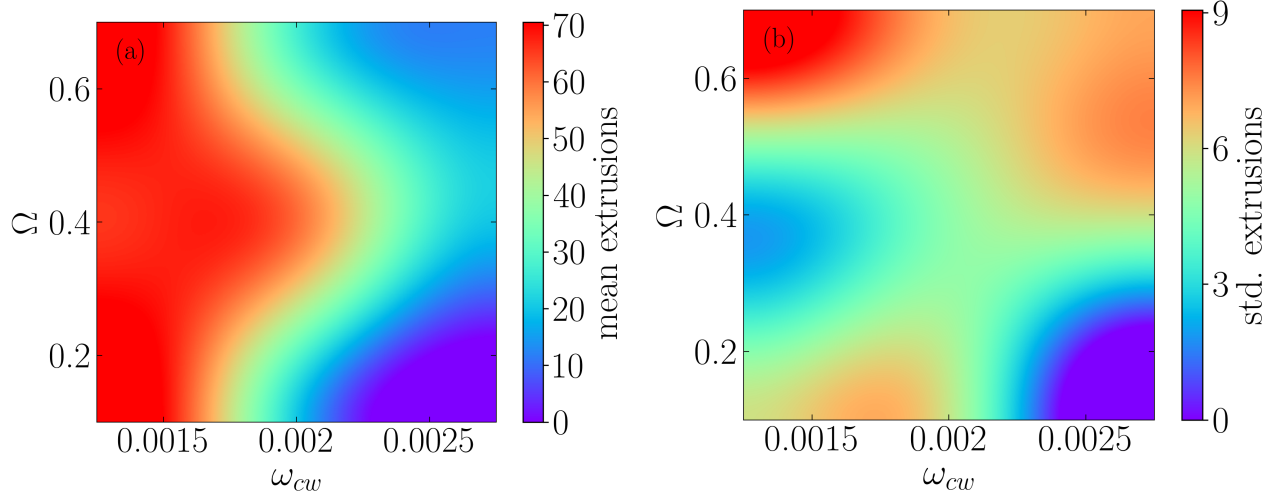


Figure 13. (a) mean and (b) standard deviation of the number of extrusions for a range of values for $\Omega = \omega_{cc}/\omega_{cw}$ and cell-substrate adhesion, ω_{cw} over the range of 29,000 time steps and for four realizations.

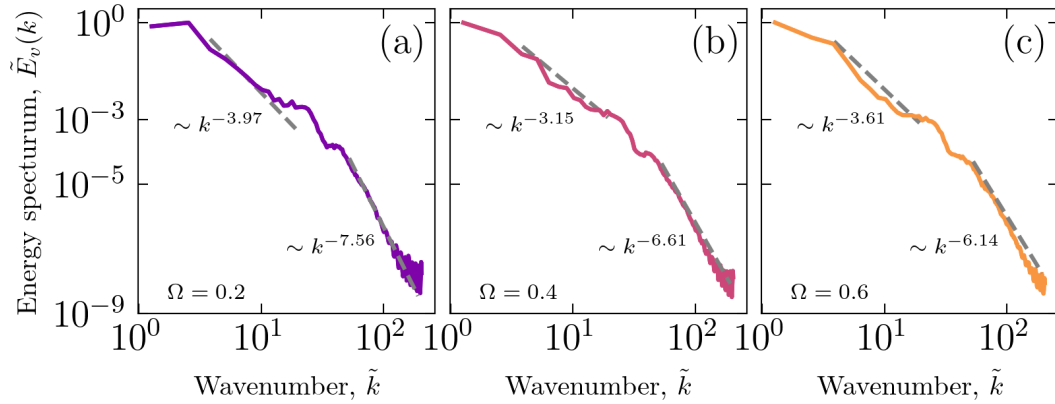


Figure 14. Energy spectra for for three sample simulations with (a) $\Omega = 0.2$, (b) $\Omega = 0.4$ and (c) $\Omega = 0.6$.

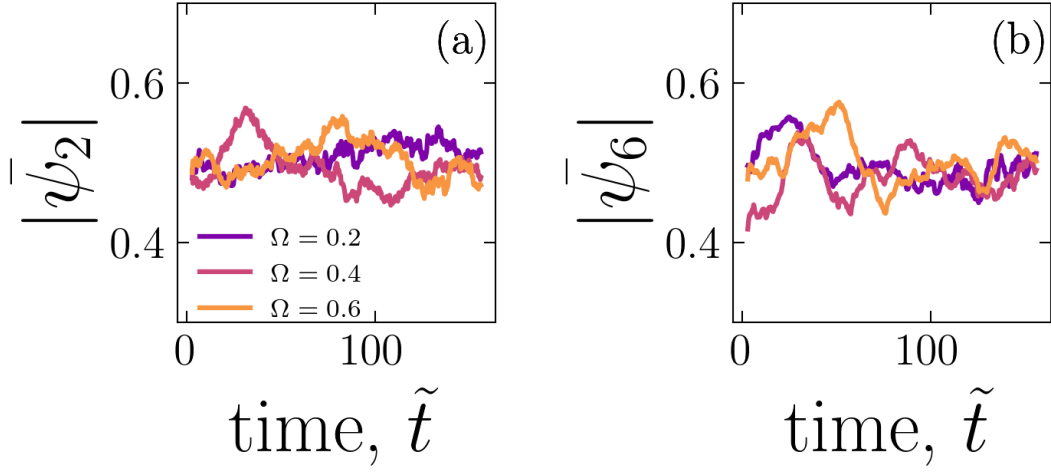


Figure 15. Temporal evolution of nematic order parameter (a) and hexatic order parameter (b) for various relative cell-cell adhesions, Ω .

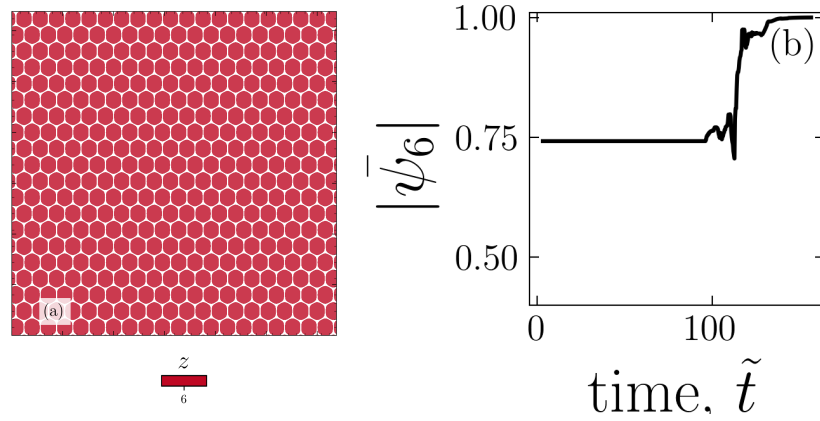


Figure 16. In absence of active forces, cells tend to equilibrate into a hexagonal lattice. An example configuration (a) and evolution of the hexatic order parameter as the systems equilibrates (b).